Supplementary Information

Wavelength-encoded microlasers for massively-multiplexed cell tagging

Nicola Martino†, Sheldon J.J. Kwok†, Andreas C. Liapis, Sarah Forward, Hoon Jang, Hwi-Min Kim, Sarah J. Wu, Jiamin Wu, Paul H. Dannenberg, Sun-Joo Jang, Yong-Hee Lee, Seok-Hyun Yun*.

† These authors contributed equally.

* Correspondence to: syun@hms.harvard.edu

Supplementary Figure 1

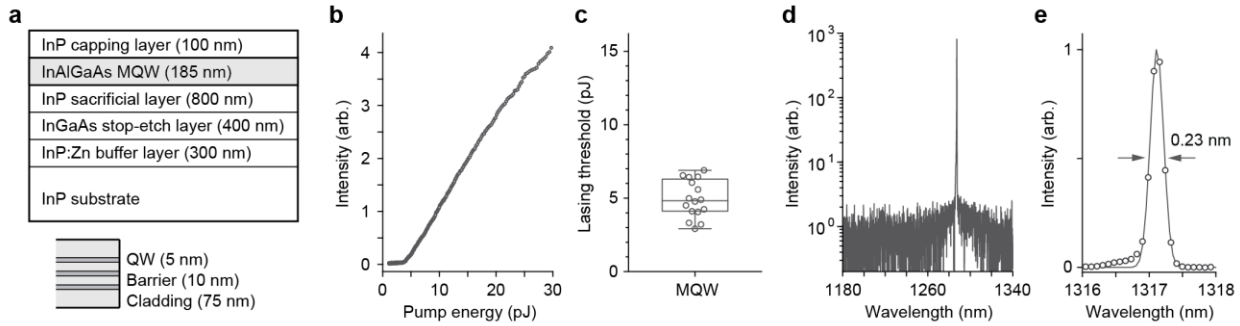

Optical characterization of MQW-based microdisks. a, Schematic diagram of the epitaxial wafer used for fabrication of MQW microdisks. **b**, Typical threshold curve (output intensity vs pump energy) of a MQW microdisk measured in air suspended on pillar. **c**, Distribution of threshold energy for MQW microdisks lasers (N = 16). **d**, Semi-logarithmic plot of a typical laser output spectrum of a typical MQW microdisk laser above lasing threshold. **e**, Gaussian fit of the linewidth of a MQW laser emission with a FWHM of 0.23 nm.

Supplementary Figure 2

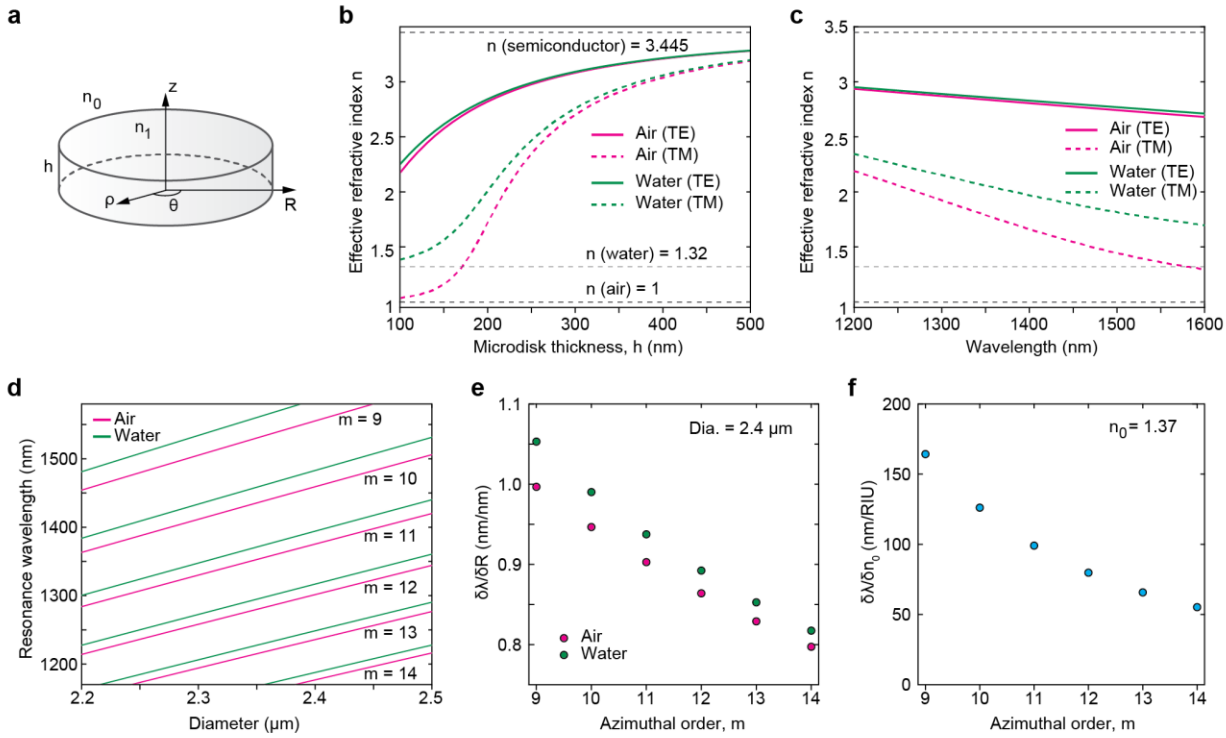

Theoretical calculation and simulations of microdisk resonances. a, Schematic of the microdisk geometry; n_0 and n_1 are the refractive indexes of the environment and semiconductor respectively, and R and h are the microdisk radius and thickness respectively. **b-c** Effective refractive index of a microdisk as a function of thickness (b) and of wavelength (c). The calculations were performed in air ($n_0 = n_{air} = 1$) and in water ($n_0 = 1.32$) for both the TE and TM modes. The refractive index of the semiconductor was set at $n_1 = 3.445$. As the resonator thickness gets smaller, the value of n_{eff} for the TM modes drops much faster than that for the TE ones. **d**, Resonance wavelengths of the TE modes for a semiconductor-only microdisk cavity (h = 200 nm) with a diameter varying from 2.2 to 2.5 μm, both in air and water, in the relevant spectral region for this work. **e**, Sensitivity of the resonance wavelength to changes in the microdisk radius, both in air and water, calculated for small variations around a design radius of R = 1.2 μm (h = 200 nm). **f**, Sensitivity of the resonance wavelength to changes in the external refractive index, calculated for small variations around the typical value in the cytoplasm n_0 = 1.37 (R = 1.2 μm, h = 200 nm).

Supplementary Figure 3

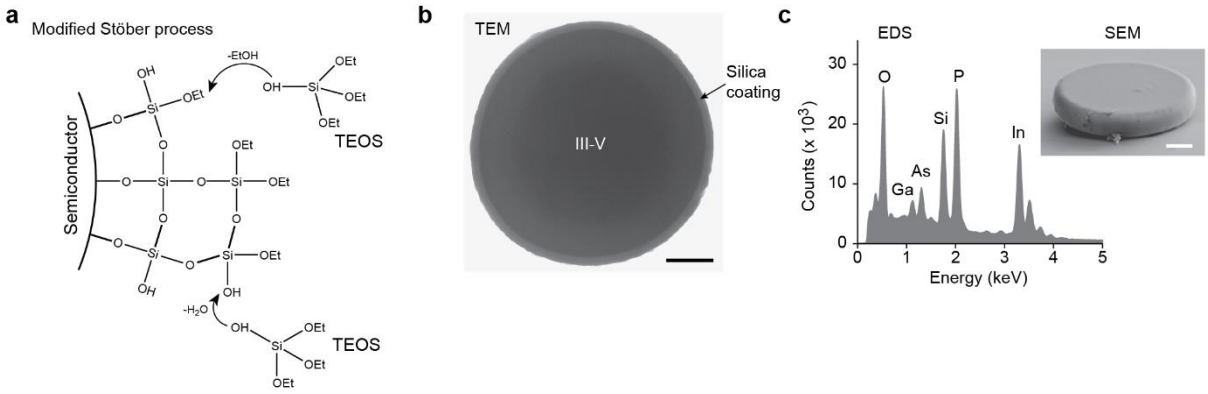

Silica coating of semiconductor microdisks. a, Schematic of the modified Stöber process for silica coating. **b**, TEM image of a coated microdisk showing the thickness and uniformity of the silica layer. Scale bar: 500 nm. **c**, EDS elemental analysis of a coated microdisk (SEM in inset, scale bar: 500 nm), demonstrating the presence of the silica shell (Si, O) around the III-V semiconductor core (In, Ga, As, P).

Supplementary Figure 4

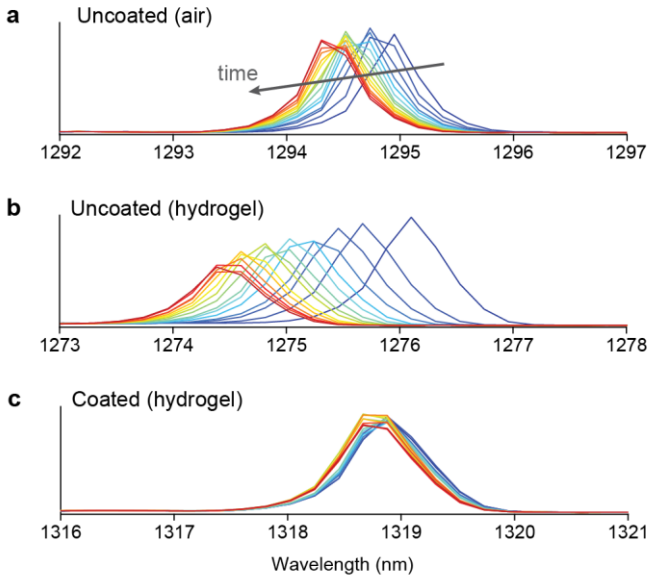

Stability of laser particles under continuous illumination. Representative spectra of microdisk emission during the degradation experiment of Fig. 4b, c for an uncoated microdisk in air (**a**), uncoated microdisk in hydrogel (**b**) and coated microdisk in hydrogel (**c**). The spectra are color coded based on time passed since the beginning of the experiment.

Supplementary Figure 5

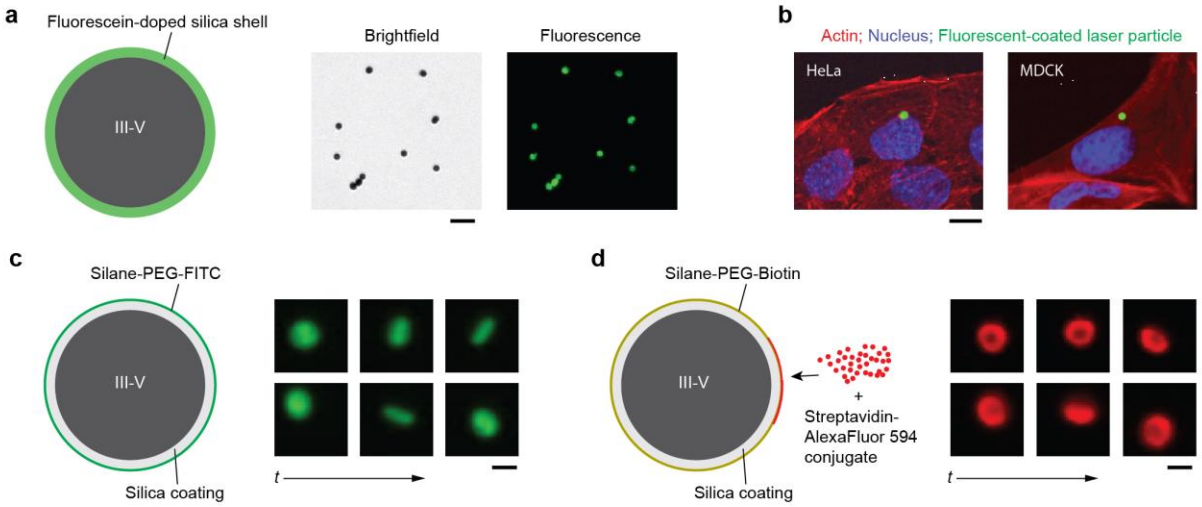

Functionalization of silica-coated laser particles. a, Fluorescent LPs were fabricated by doping the silica shell with fluorescein dyes (see Methods). Brightfield and fluorescence images of LPs showing green fluorescence from the fluorescein-doped silica shell. **b,** Fluorescence image of cells containing green-fluorescent LPs. Fixed HeLa and MDCK-II cells were stained with Alexa Fluor 594 Phalloidin (actin: red), and DAPI (nucleus: blue). Scale bar, 10 µm. **c-d**, Functionalization of silica coated LPs with poly(ethylene glycol)-fluorescein (PEG-FITC) or PEG-biotin. To confirm biotinylation, a red fluorescent streptavidin conjugate was added (d). Fluorescence images confirm encapsulation of the LPs with PEG (green, c), and biotin (red, d). Fluorescence time-lapse images show LPs undergoing Brownian motion in aqueous solution. Scale bar, 2 µm.

Supplementary Figure 6

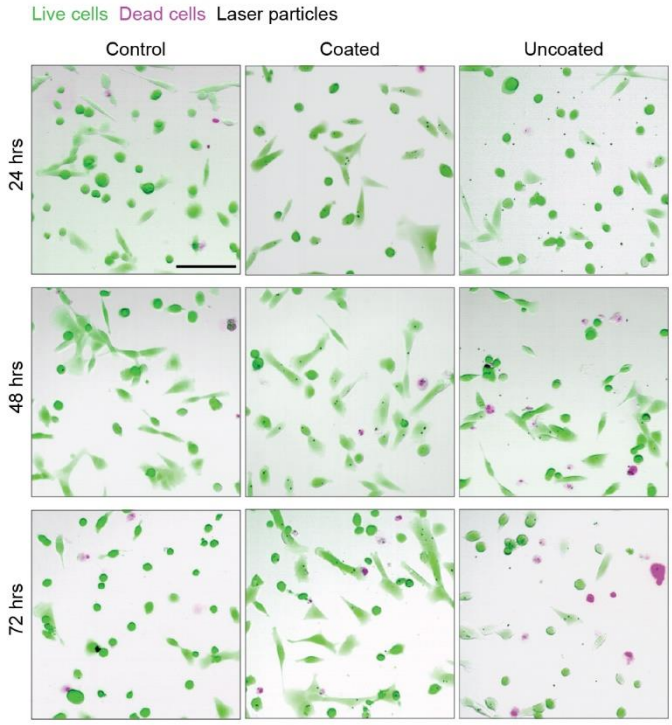

Live/dead imaging of cells with intracellular laser particles. Live/dead fluorescence staining of MDCK-II cells after incubation with coated, uncoated and no LPs (control) for 24, 48 and 72 h. Live cells and dead cells are labelled green (calcein-AM) and red (ethidium homodimer-1), respectively. Quantification of this data (*N* = 12 images per condition, about 100 cells per image) is shown in Fig. 4f. Scale bar: 100 µm.

Supplementary Figure 7

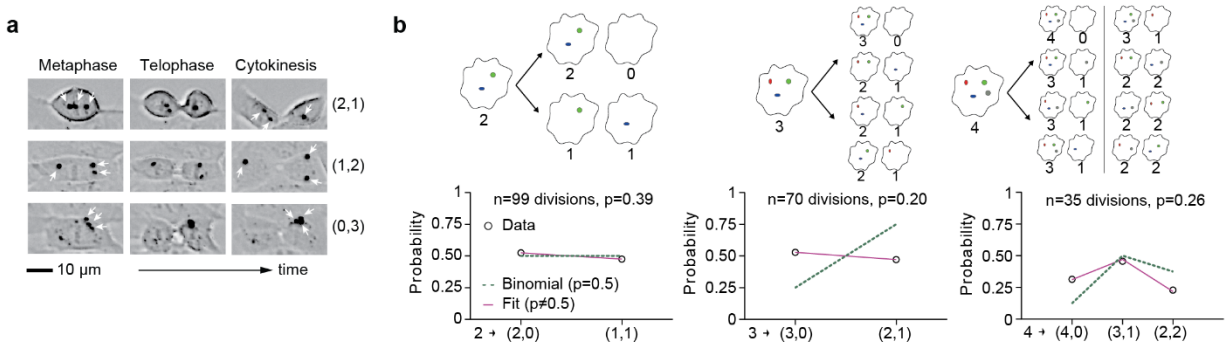

Mitotic partitioning of laser particles. a, Brightfield time-lapse images of MDCK-II cells showing mitotic partitioning of internalized LPs. Three examples are shown, where three particles (arrows) inside a single mother cell are transferred to two daughter cells at different ratios, 2:1 (1:2) or 0:3. Scale bar: 10 µm. **b**, Analysis of intracellular LPs segregation with cell division. Cell division events of MDCK-II cells containing 2, 3 or 4 LPs were annotated. The data (open black circles) shows the probability of different cell division events (e.g. 3 → (2,1) indicates that the parent cell contains 3 LPs, and the daughter cells receive 2 and 1 respectively). The dotted green line shows the expected binomial probabilities assuming the probability of transmission to either daughter cell is equal (p = 0.5). The magenta line shows fitting of the experimental data to an asymmetric binomial distribution.

Supplementary Figure 8

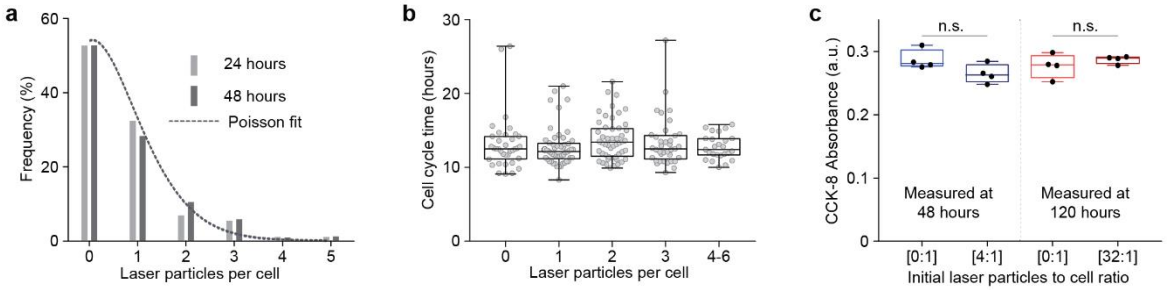

Biocompatibility of laser particles. a, Histogram of the number of LPs internalized by MDCK-II cells at 24 hours (*N* = 345 cells) and 48 hours (*N* = 303 cells), in serum-free media to minimize diluting effects of cell division. **b**, Cell cycle time measured for 201 cells carrying different numbers of LPs using time-lapse imaging. A one-way ANOVA [$F(4,197) = 1.021$] for the effect of particle number was not significant ($p > 0.05$). **c**, Effect of LPs on cellular proliferation measured by the CCK-8 assay. MDCK-II cells were incubated with 4:1 particle:cell ratio (measured at 48 h), and incubated with 32:1 ratio (measured at 120 h), compared to controls (no LPs). A two-tailed, unpaired t-test revealed no significant difference in proliferation rate between cells with and without LPs ($p > 0.05$, N = 4 for each condition).

Supplementary Figure 9

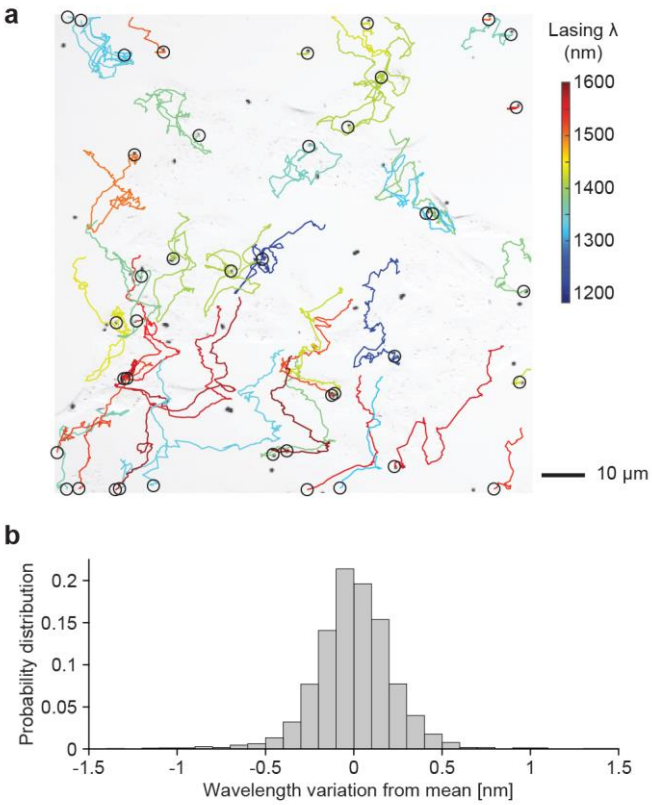

Biocompatibility of laser particles. a, Time-lapse wavelength-position traces of individual LPs superimposed with a brightfield transmission image of the MDCK cell culture. Measurements were taken every 10 min over a duration of 33 h. Circles indicate the initial positions of LPs, and the color of each traces represents lasing wavelength. **b**, Distribution of the variations in the measured wavelength at each time point from the mean value during the 33 hours tracking. Only data for LPs that were inside cells for the entire duration of the experiment are reported.

Supplementary Figure 10

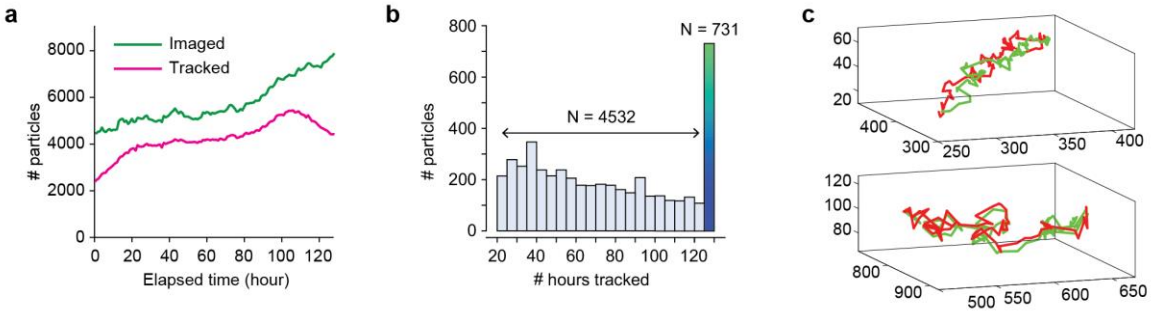

Imaging laser particles in a tumor spheroid. a, Number of LPs imaged at each time point during the time-lapse imaging of the tumor spheroid, compared to the ones that are tracked (only particles that were tracked for more than 24 hours are considered). **b**, Histogram of tracking time for all tracked LPs. **c**, Example of two LPs following the same paths throughout their entire tracking duration. Such particles were considered as being in the same cell and merged into a single trace.

Supplementary Figure 11

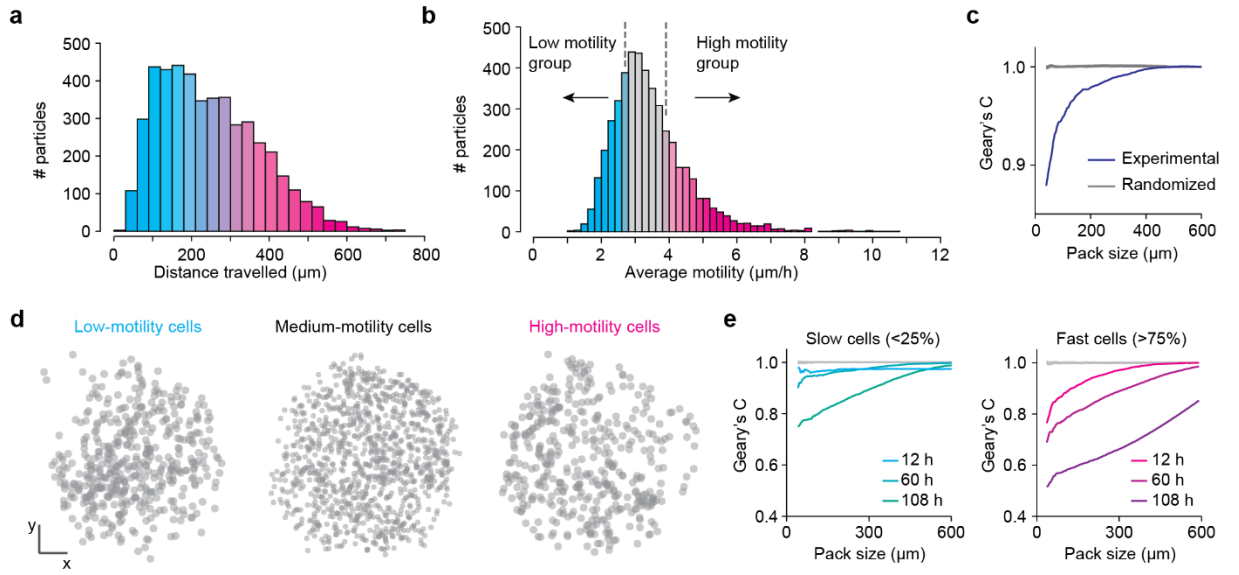

Motility analysis of LP-tagged cells. a, Statistics of the traveled distance for each cell during the tracking time, calculated as the (scalar) sum of the displacements at each time interval. **b**, Statistics of average motility for each tracked cell, calculated as total travel distance divided by tracking time. The low- and high-motility cells were determined as the bottom and top quartile of the histogram, respectively, and the remaining cells are classified as medium motility. **c**, Geary's coefficient computed for spatial autocorrelation of overall motility to initial cellular coordinates, presented as a function of cellular pack size. The randomized control is computed by random assignment of motilities to cells, and the 95% confidence interval of 100 simulations is shown. The difference between experimental and randomized data indicates strong spatial autocorrelation below approximately 200 μm. **d**, Position at early times (t = 12 h) of low, medium and high motility cells within the spheroid. Scale bars, 100 μm. **e**, Geary's coefficient computed for spatial autocorrelation of instantaneous velocities to cellular position at given times. Slow and fast cells represent the bottom and top quartiles of instantaneous velocities at each time, respectively. Randomized control (95% confidence interval of 100 simulations) is shown for each group. The data indicates significantly higher spatial autocorrelation for fast cells before (12 h), at the onset (60 h) and during (108 h) invasion.

Supplementary Figure 12

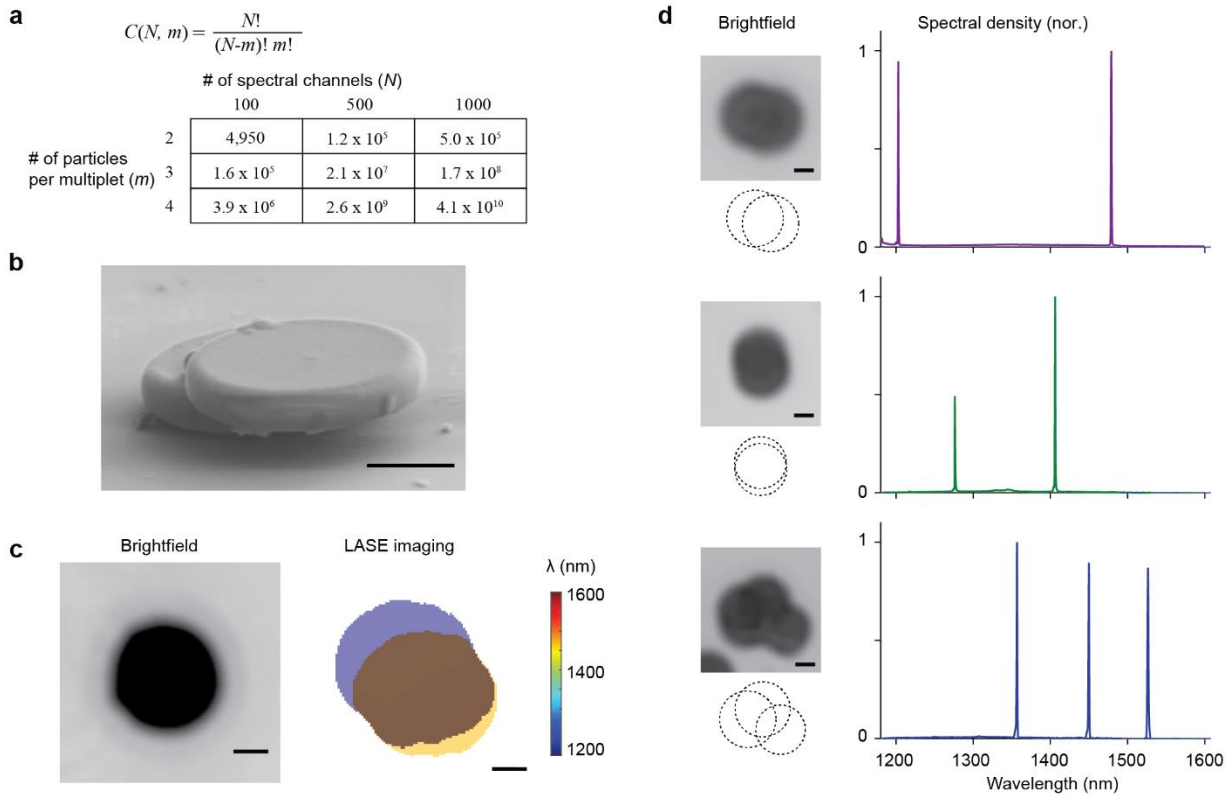

Multiplet microdisk laser particles. a, Theoretical number of uniquely identifiable spectra or optical barcodes when multiple laser particles are combined to form a multiplet. The number of unique combinations is given for the # of particles per multiplet (*m*) and the number of distinguishable spectral channels (*N*). **b**, SEM image of a multiplet that was formed after three cycles of silica coating. Multiple cycles of Stöber coating results in occasional formation of laser particle aggregates. The silica coating thickness is approximately 150 nm. Scale bar: 1 µm, **c**, Brightfield and LASE image of a laser particle doublet. Lasing peaks were observed at 1197 nm, 1491 nm or both, depending on the spatial overlap of each disk in the multiplet and the pump beam. Scale bars: 1 µm. **d**, Brightfield images and emission spectra of doublet and triplet particles formed during multiple coating cycles. Scale bars: 1 µm.

Supplementary Videos

Supplementary Video 1: Macropinocytosis of microdisk laser particles

This video shows uptake of microdisk laser particles by MDCK-II cells.

Supplementary Video 2: Time-lapse brightfield imaging of intracellular laser particles

This video shows laser particle uptake by MDCK-II cells, and their migration and proliferation behaviors over several days of imaging at 5 minute intervals.

Supplementary Video 3: Time-lapse brightfield imaging of intracellular laser particles

This video shows laser particle uptake by MDCK-II cells, and their migration and proliferation behaviors over several days of imaging at 5 minute intervals. One particular cell in the upper part of the video is shown to uptake more than 10 particles and subsequently undergoes apoptosis.

Supplementary Video 4: Time-lapse brightfield imaging of intracellular laser particles

This video shows the uptake of one laser particle by a MDCK-II cell. At approximately t = 2.5 h, the laser particle appears to leave the cell momentarily. However, prior to t = 3 h, the laser particle may not be completely internalized and appears to be resting within the lamellipodium or cell surface. Following t = 3 h, the laser particle is completely internalized, and the cell successfully divides (t = 13 h), passing the particle to one of its daughter cells. We were not able to identify any clear evidence of exocytosis in our imaging data.

Supplementary Video 5: Time-lapse imaging of spheroid evolution

This video shows the time-lapse brightfield imaging collected during the 4T1 spheroid invasion assay (one frame every hour for 128 hours). The spheroid is observed growing in size at early times (up to 40 hours), and then cells start to invade the surrounding matrix.

Supplementary Video 6: Time-lapse imaging of individual cell movement in spheroid invasion assay

This video shows the instantaneous velocities of the tracked cells at each time point during the time-lapse imaging of the spheroid invasion assay. Each arrow represents the (vector) velocity of a single laser particle, color coded by its magnitude.

Supplementary Notes

Supplementary Note 1: WGM resonance modeling

Resonance wavelengths for bare microdisk resonators of different diameters were calculated using the effective index method[1] for a cylindrical resonator of radius *R*, thickness *h* and refractive index n_1 in an environment with refractive index n_0 (Supplementary Fig. 2a). The original 3-dimensional problem can be approximated to a 2D disk of effective refractive index $n_{eff}(\lambda)$, given for TE and TM modes by the solution of the implicit equations:

$$TE:\ tan\left(\frac{\pi h}{\lambda}\sqrt{n_1^2 - n_{eff}^2}\right) = \sqrt{\frac{n_{eff}^2 - n_0^2}{n_1^2 - n_{eff}^2}} \qquad (S1)$$

$$TM:\ tan\left(\frac{\pi h}{\lambda}\sqrt{n_1^2 - n_{eff}^2}\right) = \frac{n_1^2}{n_0^2}\sqrt{\frac{n_{eff}^2 - n_0^2}{n_1^2 - n_{eff}^2}} \qquad (S2)$$

These equations may have more than one solutions corresponding to different thickness modes of the disk. The maximum thickness h_{sm}, below which only the fundamental thickness mode is supported, is given by:

$$h_{sm} = \frac{\lambda}{2\sqrt{n_1^2 - n_0^2}} \qquad (S3)$$

For a design wavelength of λ = 1350 nm and n_1 = 3.445, we obtain h_{sm} = 205 nm in air (n_0 = 1) and h_{sm} = 212 nm in water (n_0 = 1.32). The actual thickness of 200 nm satisfies the single-mode condition, $h < h_{sm}$.

We calculated the effective refractive indices of only the lowest-order TE and TM modes, as shown in Supplementary Fig. 2b, c. The TE modes have considerably higher n_{eff} than the TM modes, especially for thicknesses below h_{sm}. We thus focused our analysis on the TE modes, which are better confined and have higher Q-factors[2]. The electromagnetic field profile of the TE modes for the 2D disk is given, in cylindrical coordinates, by[1]:

$$H_z = \begin{cases} AJ_m\left(k_0 n_{eff}\rho\right)e^{-i(m\phi-\omega t)}, & \rho \le R \\ BH_m^{(2)}(k_0 n_0 \rho)e^{-i(m\phi-\omega t)}, & \rho > R \end{cases} \qquad (S4)$$

$$E_\rho = \frac{j\mu_0\omega}{k_0^2 n^2 \rho}\frac{\partial H_z}{\partial \rho}, \qquad E_\phi = -\frac{j\mu_0\omega}{k_0^2 n^2}\frac{\partial H_z}{\partial \rho}, \qquad E_z = H_\rho = H_\phi = 0$$

where J_l is the Bessel function of the first kind, $H_l^{(2)}$ is the Hankel function of the second kind, μ_0 is the vacuum permeability, m is the azimuthal order of the mode, A and B are normalization constant, ω and k_0 are the frequency and wavenumber. By applying the boundary conditions at the disk edge, i.e. the continuity of E_φ and H_z, we can derive the following relationship:

$$\frac{J_{m-1}(U) - J_{m+1}(U)}{UJ_m(U)} = \frac{H_{m-1}^{(2)}(Q) - H_{m+1}^{(2)}(Q)}{QH_m^{(2)}(Q)} \qquad (S5)$$

where we have defined $U = k_0 n_{eff} R$ and $Q = k_0 n_0 R$. As both Eq. (S1) and Eq. (S4) depend only on n_{eff} and λ, they can be solved together to find the resonance wavelengths $\lambda_{m,p}$, where p is the radial order of the modes. The solutions for the resonance modes of microdisks with varying diameters are reported in Supplementary Fig. 2d, for both air and water as the external medium.

This model allows us to estimate how much the resonance wavelengths of the cavities are affected by changes in the various parameters of the problem. For microdisks of 2 μm in diameter (Fig. 1c), the sensitivity to small variations in microdisk radius id $\delta\lambda/\delta R$ = 1.07 and 1.01 nm/nm respectively for m = 9 and 10. For diameters in the 2.2 – 2.5 μm range (Fig. 2) the $\delta\lambda/\delta R$ ranges from 0.8 to 1.05 nm/nm as shown in Supplementary Fig. 2e.

The sensitivity of the resonance wavelength to small variations in external refractive index ($\delta\lambda/\delta n_0$) at a design radius of 1.2 μm is shown in Supplementary Fig. 2f. $\delta\lambda/\delta n_0$ varies from 160 nm/RIU for m = 9 to 50 nm/RIU for m = 14.

Supplementary Note 2: Errors in laser particle identification

Consider a series of laser particles (i''s) with incrementally increasing nominal wavelengths $\lambda_{0,i}$ with an interval of Δ. We assume that spectral measurement has a Gaussian distribution with a standard deviation σ. When $\Delta \gg \sigma$, the series of particles can be correctly identified by ranking the measured wavelengths in increasing order. However, a finite probability for error exists when the measured rank order between two adjacent particles is reversed due to the measurement uncertainty. The probability that a single measurement of the i-th particle will yield a value λ_i is described by a probability density function P_i:

$$pdf_i(\lambda_i) = \frac{1}{\sqrt{2\pi}\sigma} e^{-\left(\frac{\lambda_i - \lambda_{0,i}}{\sqrt{2}\sigma}\right)^2} \qquad (S6)$$

For correct identification, the measured wavelength λ_i the i-th particle should fall between the measured values of the (i-1)-th and (i+1)-th particles, i.e. $\lambda_{i-1} < \lambda_i < \lambda_{i+1}$. When $\Delta\lambda \gg \sigma$, the dominant error is due to nearest neighbor swapping, which occurs when $\lambda_i < \lambda_{i-1}$ or $\lambda_i < \lambda_{i+1}$. The probability of this mismatching error is given:

$$E(\lambda_i) = P[\lambda_i < \lambda_{i-1}] + P[\lambda_i > \lambda_{i+1}] \qquad (S7)$$

The total error probability P_{err} of incorrectly assigning the i-th particle is expressed as:

$$P_{err} = \int_{-\infty}^{+\infty} pdf_i(\lambda_i) E(\lambda_i) d\lambda_i = \int_{-\infty}^{+\infty} pdf_i(\lambda_i) \left[\int_{\lambda_i}^{+\infty} pdf_{i-1}(\lambda) d\lambda + \int_{-\infty}^{\lambda_i} pdf_{i+1}(\lambda) d\lambda \right] d\lambda_i \qquad (S8)$$

Using $(S6)$, we find:

$$P_{err} = 1 - erf\left(\frac{\Delta}{2\sigma}\right) \qquad (S9)$$

where erf is the error function. For Δ = 1 nm and σ = 0.18 nm, we obtain P_{err} = 8.6x10^{-5}.

Another way of identifying laser particles is to assign fixed bins of a width equal to Δ around the nominal wavelengths $\lambda_{0,i}$ and match the measured value λ_i to a corresponding bin. The probability of error in this case is given by:

$$P_{err} = \int_{-\infty}^{\lambda_{0,i}-\Delta/2} pdf_i(\lambda) d\lambda + \int_{\lambda_{0,i}+\Delta/2}^{+\infty} pdf_i(\lambda) d\lambda \qquad (S10)$$

Therefore, we find:

$$P_{err} = 1 - erf\left(\frac{\Delta}{2\sqrt{2}\sigma}\right) \qquad (S11)$$

For Δ = 1 nm and σ = 0.18 nm, we have in this case P_{err} = 5.5x10^{-3}.

References

1. Andronico, A. *et al.* Semiconductor microcavities for enhanced nonlinear optics interactions. *J. Eur. Opt. Soc. Rapid Publ.* **3,** 08030 (2008).
2. Frateschi, N. C. & Levi, A. F. J. The spectrum of microdisk lasers. *J. Appl. Phys.* **80,** 644–653 (1996).